INTERNATIONAL JOURNAL OF HYDROGEN ENERGY 36 (2011) 6768–6779

Available at www.sciencedirect.com

ScienceDirect

journal homepage: www.elsevier.com/locate/he

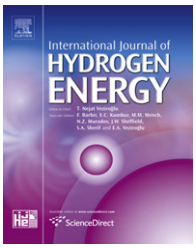

Preferential oxidation of CO in H_2-rich feeds over mesoporous copper manganese oxides synthesized by a redox method

Eric C. Njagi [a], *Homer C. Genuino* [a], *Cecil K. King'ondu* [a], *Chun-Hu Chen* [a], *Dayton Horvath* [a], *Steven L. Suib* [a,b,*]

[a] *Department of Chemistry, University of Connecticut, Storrs, CT 06269-3060, USA*
[b] *Department of Chemical, Materials and Biomolecular Engineering, University of Connecticut, U-3060, 55 North Eagleville Rd., Storrs, CT 06269-3060, USA*

ARTICLE INFO

Article history:
Received 10 November 2010
Received in revised form
11 February 2011
Accepted 17 February 2011
Available online 12 March 2011

Keywords:
Preferential CO oxidation
PEM fuel cell
Copper manganese oxide
Hydrogen

ABSTRACT

Mesoporous copper manganese oxides with high surface areas (>268 m^2/g) were prepared using the redox method and tested in the preferential oxidation of CO. These materials were highly active and selective under typical operating conditions of a proton-exchange membrane fuel cell. The synthesized catalysts preferentially oxidized CO with a stoichiometric amount of oxygen in the feed gas. The presence of CO_2 and H_2O in the feed gas retarded catalytic activity significantly at low (<90 °C) temperatures. The catalysts showed stable activity in long-term (12 h) experiments with realistic feeds. The high catalytic activity was attributed to a combination of factors, including high surface area, low crystallinity, low activation energy for CO oxidation, compositional homogeneity of the copper manganese oxides, and the presence of readily available lattice oxygen for CO oxidation. The high selectivity (100% with stoichiometric reactants) was ascribed to the lower activation energy for CO oxidation compared to the activation energy for H_2 oxidation.

1. Introduction

Low temperature (80–100 °C) polymer electrolyte membrane (PEM) fuel cells have attracted considerable interest due to their potential use as an alternative energy source for both mobile and stationary applications. The efficiency, high energy and power densities obtainable in H_2-fueled PEM fuel cells coupled with benign tailpipe emissions make them very attractive power sources for electric vehicles, and small-scale energy devices [1–3]. The PEM fuel cell is designed to operate using hydrogen gas produced by reforming of methanol or hydrocarbon fuels, and the feed gas typically contains 45–75 vol.% H_2, 15–25 vol.% CO_2, 0.5–2 vol.% CO, and a few vol.% H_2O [4]. Although the PEM cell is completely CO_2 tolerant, the anode is highly susceptible to CO poisoning with consequent voltage losses [5,6]. Thus, the total concentration of CO in the gas stream should be reduced to below 10 ppm in order to obtain optimum performance [7].

Several approaches have been investigated to remove CO from H_2-rich streams including selective diffusion, methanation, and preferential CO oxidation. Preferential oxidation of CO (PROX) is one of the most promising cost-effective methods of reducing the concentration of CO to acceptable levels especially for automotive applications [8,9]. There are two temperature levels that are ideal for the PROX reaction: the fuel cell operating temperature (80–100 °C) or the temperature level of the reformer unit (250–300 °C).

* *Corresponding author*. Department of Chemistry, University of Connecticut, Storrs, CT 06269-3060, USA. Tel.: +1 860 486 2797; fax: +1 860 486 2981.
E-mail address: steven.suib@uconn.edu (S.L. Suib).
0360-3199/$ – see front matter
doi:10.1016/j.ijhydene.2011.02.097

Catalysts reported to be active for the PROX reaction are broadly divided into three groups namely; supported noble metals, metal oxides and mixed metal oxides. Supported Pt [10–15], Ru [16–18], and Rh [19–21] catalysts have good catalytic activity and moderate selectivity in the temperature range of 150–250 °C. Supported gold catalysts have been reported to be highly active and selective at low temperatures (<100 °C) but they are highly susceptible to CO_2 poisoning [22–28]. Moreover, the selectivity of supported gold catalysts rapidly decreases with reaction temperature.

Among the mixed metal oxides the CuO–CeO_2 system has been intensively studied and found to be quite active and selective for the PROX reaction [4,29–35]. The drawbacks of CuO–CeO_2 catalysts include their low activity and selectivity at high space velocities, and their poor resistance to deactivation by water. Cobalt oxide (CoO) has been reported to show the best performance among the metal oxides and completely oxidized CO at 100 °C with high selectivity (~ 90%) in the absence of CO_2 and H_2O [36].

There still exists a need to develop stable cost-effective catalysts for the PROX reaction with high activity, selectivity, and tolerance to CO_2 and H_2O. Mixed copper manganese oxide catalysts have been extensively used to remove CO from breathing air due to their low cost. However, they have not been widely studied for the PROX reaction presumably due to their low catalytic activity at near ambient temperatures and their rapid deactivation by moisture [37–40]. Recently, Hasegawa et al. [41] have synthesized copper manganese oxides using the sol-gel method and found them to be highly active and selective for PROX at temperatures below 100 °C. A nanosized copper manganite ($CuMn_2O_4$) catalyst synthesized via the silica aquagel confined co-precipitation method was active for preferential oxidation of CO but deactivated during the reaction [42]. Additionally, Hernández and co-workers [43] have synthesized copper modified cryptomelane-type manganese dioxide nanomaterials via the milling method and found them to be active for the preferential oxidation of CO at high (140–180 °C) temperatures. However, in the afore-mentioned studies the feed gas did not contain CO_2 and H_2O (two components of reformate gas that have deleterious effect on catalytic conversion).

In our previous study [44] we prepared copper manganese oxides using a novel redox method and found them to have excellent catalytic activity for CO oxidation at ambient temperatures. Moreover, they were significantly better at withstanding moisture than commercial copper manganese oxides. In our present work, amorphous manganese oxide and binary copper manganese oxides synthesized by the afore-mentioned method are examined for their activities and selectivities for the PROX reaction using a realistic feed gas. The influence of the presence of 25% CO_2 and 3% H_2O in the feed gas on the catalytic activity, selectivity, and stability is also investigated.

2. Experimental

2.1. Preparation of catalysts

Amorphous manganese oxide (AMO) and binary copper manganese oxides were synthesized using a redox method described previously [44]. Briefly, AMO was prepared by the dropwise addition of 1.80 M solution of manganese (II) acetate tetrahydrate ($Mn(CH_3COO)_2{\cdot}4H_2O$, Alfa Aesar; AR) to an equal volume of 1.20 M potassium permanganate ($KMnO_4$, Fisher Scientific; 99.3%) under vigorous stirring. The resultant precipitate was stirred continuously for 24 h, filtered, washed, vacuum dried, and ground into powder. The afore-mentioned procedure was modified slightly to prepare binary copper manganese oxide precursors with nominal copper/manganese molar ratios of 5/95, 10/90, and 15/85 by adding appropriate amounts of copper (II) nitrate hemihydrate ($Cu(NO_3)_2.2.5H_2O$, Mallinckrodt Baker; AR) to the manganese (II) acetate solution before reduction. The copper manganese oxide precursors were calcined in air for 2 h at 300 °C and the resultant samples designated $CuMnO_{x-5}$, $CuMnO_{x-10}$, and $CuMnO_{x-15}$ based on the nominal copper content.

2.2. Characterization of catalysts

The morphology of the samples was studied by field emission scanning electron microscopy (FE-SEM) and transmission electron microscopy (TEM). The FE-SEM micrographs were taken using a JEOL JSM-6335F microscope at an accelerating voltage of 10.00 kV and a beam current of 12 μA. Samples were prepared for analysis by dispersing them in ethanol and coating a monolayer on a silicon wafer. The low-resolution TEM (LR-TEM) images, selected area electron diffraction (SAED) patterns, and elemental maps were obtained with a FEI Tecnai T12 TEM/STEM equipped with an energy dispersive (EDS) detector at an accelerating voltage of 120 kV. High-resolution TEM (HR-TEM) images were recorded with a JEOL 2010 FasTEM microscope operating at an accelerating voltage of 200 kV. Samples were ultrasonically dispersed in ethanol. A drop of the resulting suspension was then deposited onto Quantafoil holey carbon-coated grids and allowed to dry before analysis.

The textural properties of the samples were determined by performing nitrogen sorption measurements using a Micrometrics ASAP 2010 instrument. The surface areas and pore size distribution were determined by the Brunauer-Emmett-Teller (BET) and the Barrett–Joyner–Halenda (BJH) methods, respectively. The adsorption and desorption experiments were done at 77 K after initial pretreatment of the samples by degassing at 150 °C for 12 h. Elemental analysis was performed using a Perkin Elmer Model 3100 flame atomic absorption spectrometer (FAAS) by standard calibration method.

Thermal analysis was performed using a TA instruments SDT Q600 TGA/DSC Thermogravimetric Analyzer. Samples were loaded into alumina pans and heated from room temperature to 1000 °C in N_2 atmosphere (100 mL/min) at a ramp rate of 20 °C/min. Gases desorbing from the samples during thermal treatment were monitored using Diablo 5000A Real-Time Gas Analyzer (RTGA) equipped with an Agilent Technologies 5975 quadrupole Mass Selective Detector (MSD). The samples were heated from room temperature to 1000 °C in a flow (100 mL/min) of UHP helium at a ramp rate of 20 °C/min.

Temperature programmed desorption/reduction (TPD/R) experiments were carried out using a Diablo 5000A real-time gas analyzer (RTGA) equipped with an Agilent Technologies 5975 quadrupole MSD detector. The catalyst (100 mg) was

packed into a quartz tube and loaded into a Carbolite® MTF model horizontal tube furnace. CO- and H_2-TPD experiments were performed using a feed gas composed of 10% CO and 10% H_2 in He, respectively. Competitive adsorption experiments were performed using a gas mixture composed of 10% CO and 10% H_2 in He. Samples were pretreated by flowing ultra high purity (UHP) He (50 sccm) for 2 h at 180 °C and then cooled to room temperature. Adsorption was then undertaken by flowing respective feed gasses for 1 h at a flow rate of 50 sccm. Samples were subsequently purged with UHP He (50 sccm) for 30 min to remove any surface physisorbed gases and residual feed gas from the streams. After purging, desorption was carried out by heating the samples under a flow of UHP He (50 sccm) from room temperature to 700 °C at a ramp rate of 10 °C/min.

The CO temperature programmed reduction (CO-TPR) experiments were performed using CO as the reducing gas. Pretreated samples were heated in a flow (50 sccm) of 1% CO in He from room temperature to 700 °C at a rate of 10 °C/min. The change in the concentration of CO was monitored using the MSD detector.

2.3. Catalytic performance tests

Catalytic tests were performed using a continuous flow fixed bed quartz tubular reactor at atmospheric pressure with 100 mg of the catalyst. The reactor temperature was measured using a K-type thermocouple in direct contact with the sample upstream of the catalyst bed and regulated by a PID temperature controller. The catalysts were pretreated by flowing UHP He (50 mL/min) at 180 °C for 2 h to completely dry and remove any adsorbed species on the surface. Preferential oxidation experiments were performed using a gas feed consisting of 1% CO, 1% O_2, 60% H_2 balanced with N_2. The effects of CO_2 and H_2O were examined by adding 25% CO_2 and ~ 3% H_2O into the feed gas, respectively. Water was added by passing the dry feed gas through a water bubbler maintained at room temperature.

The feed and product gas streams were analyzed by a SRI 8610C gas chromatograph (GC) equipped with a 6′ molecular sieve, a 6′ silica gel column, and a thermal conductivity detector (TCD). Catalytic data were collected after allowing 30 min stabilization at each analysis temperature. Methane formation was not detected under our experimental conditions. The CO conversion and selectivity of O_2 to CO oxidation were defined as:

$$\text{CO conversion}\left(\%\right) = \frac{[CO]_{in} - [CO]_{out}}{[CO]_{in}} \times 100$$

$$\text{Selectivity}\left(\%\right) = 0.5\frac{\left([CO]_{in} - [CO]_{out}\right)}{\left[O_2\right]_{in} - \left[O_2\right]_{out}} \times 100$$

3. Results

3.1. Characterization of the catalysts

In our previous study [44] AMO and copper manganese oxides synthesized using the redox method were characterized using the XRD method and found to be amorphous. In addition, the

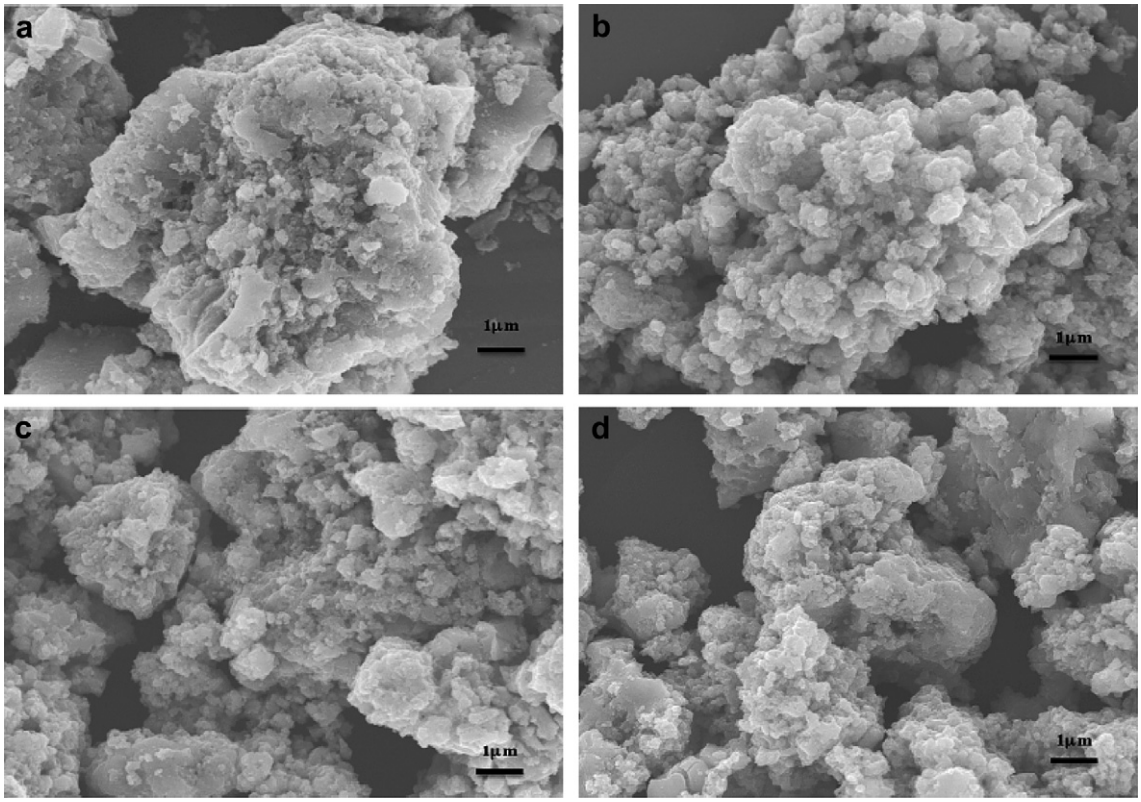

Fig. 1 – The FE-SEM images of:(a) AMO (b) $CuMnO_{x-5}$ (c) $CuMnO_{x-10}$, and (d) $CuMnO_{x-15}$ samples.

XRD patterns lacked diffraction peaks corresponding to crystalline copper oxide suggesting that the copper species were either highly dispersed or in an amorphous state [45]. Results of further characterization studies are presented in the following sections.

3.1.1. *Morphology*

Fig. 1 shows the FE-SEM images of samples prepared using the redox method. The micrographs reveal these materials are composed of aggregates of near-spherical microparticles. A closer examination (Fig. 2(a, b)) of the aggregates using low-resolution TEM reveal they are composed of fibrous nanoscale particles of relatively uniform size and dimensions. The selected area electron diffraction (SAED) patterns (insets of Fig. 2(a, b)) lack diffraction rings or spots, which is consistent with the amorphous nature of these materials. High-resolution TEM (Fig. 2(c, d)) analysis shows these materials are composed of nanoparticles of relatively uniform size (5–10 nm).

The scanning transmission electron microscopy (STEM) images of the $CuMnO_{x-10}$ sample are shown in Fig. 3. These elemental maps show that the distribution of Cu, Mn, and O is largely uniform indicating a high compositional homogeneity. The STEM analysis could not resolve the elemental composition of individual particles in the sample. However, when considered together with TEM, and elemental analysis data (*vide infra*), the STEM results suggest an intimate intermixing of Cu, Mn, and O in the copper manganese oxides.

3.1.2. *Thermal stability*

The TGA plots of materials prepared using the redox method are shown in Fig. 4. There are three major weight losses in the TGA profiles between 25 and 1000 °C. The first major weight loss occurred between 25 and 250 °C. The second major weight loss occurred between 250 and 500 °C while the third major weight loss occurred between 500 and 1000 °C. AMO and

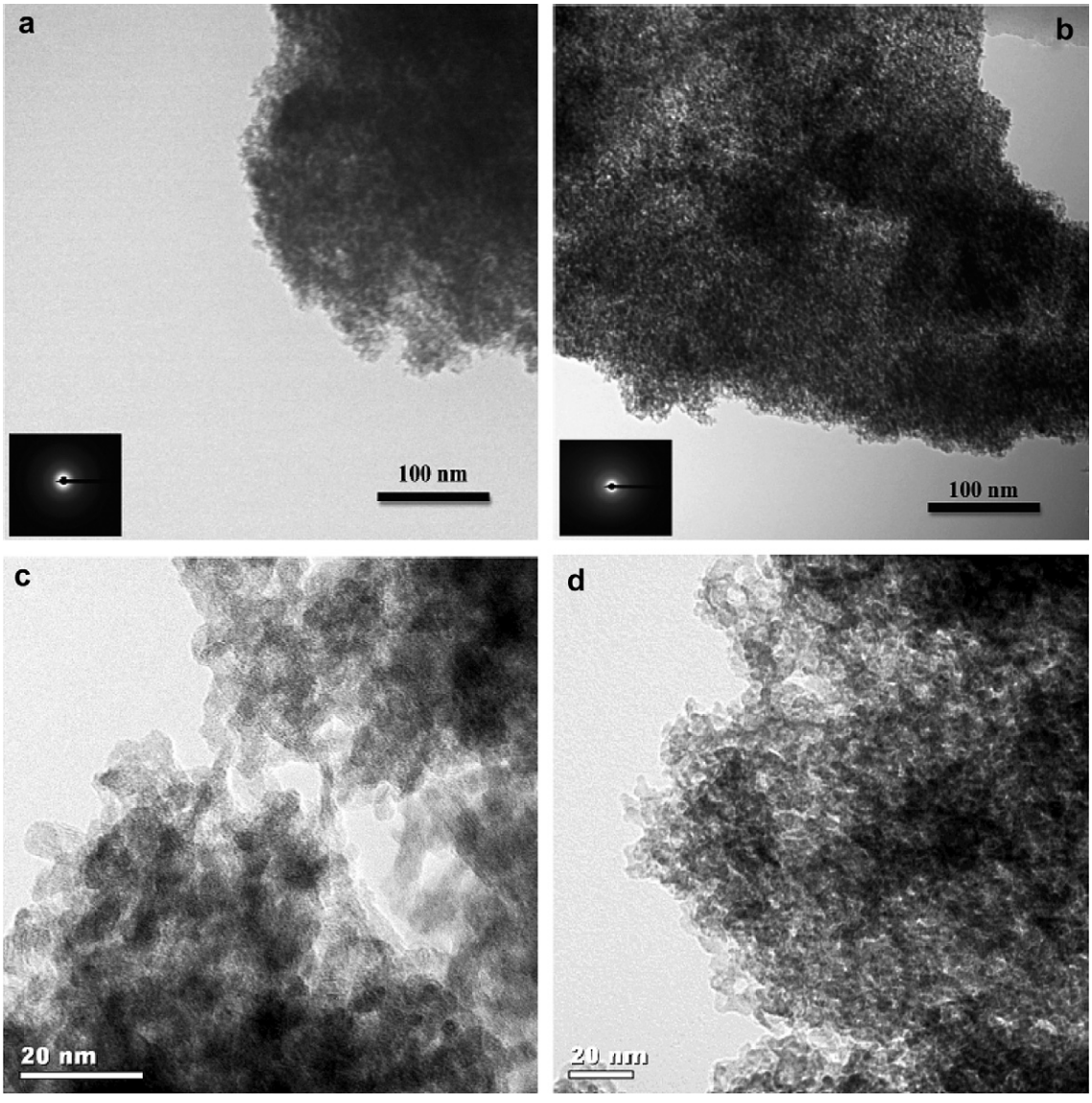

Fig. 2 – Low-resolution TEM images of: (a) AMO (b) $CuMnO_{x-10}$ and high-resolution TEM images of: (c) AMO (d) $CuMnO_{x-10}$ samples.

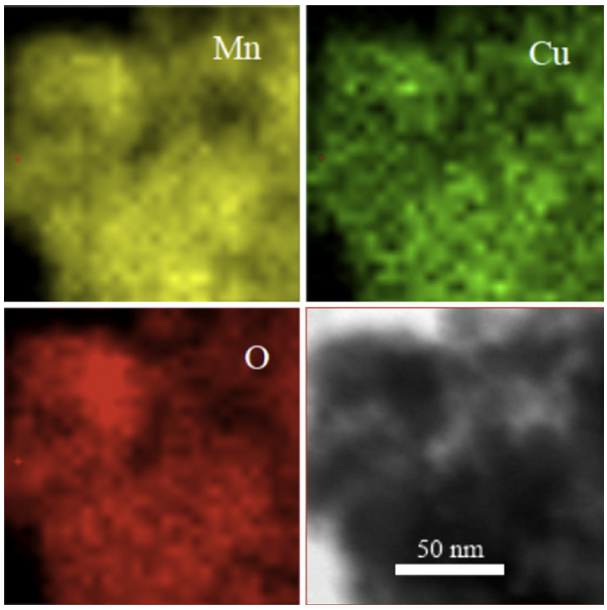

Fig. 3 – The STEM elemental maps showing the distribution of Mn, Cu, and O in the $CuMnO_{x-10}$ sample and the corresponding STEM image.

$CuMnO_{x-5}$ samples show two additional major weight losses between 800 and 1000 °C. A slight weight gain was observed between 500 and 800 °C. The cause of this weight gain is currently unclear. The thermal behavior of AMO and $CuMnO_{x-5}$ samples was similar, the only difference being the degree of weight loss in these temperature ranges. Likewise, $CuMnO_{x-10}$ and $CuMnO_{x-15}$ showed similar thermal behavior. The TGA results indicate that these materials are thermally stable at PEM fuel cell operating conditions.

The corresponding DSC profiles of AMO and copper manganese oxides are shown in Fig. 5. Both exothermic and endothermic heat flows associated with mass loss are observed. However, no heat flows associated with phase transitions are observed in the DSC profiles. The endothermic peaks (25–250, 850, and 920 °C) are associated with weight loss in these temperature regions.

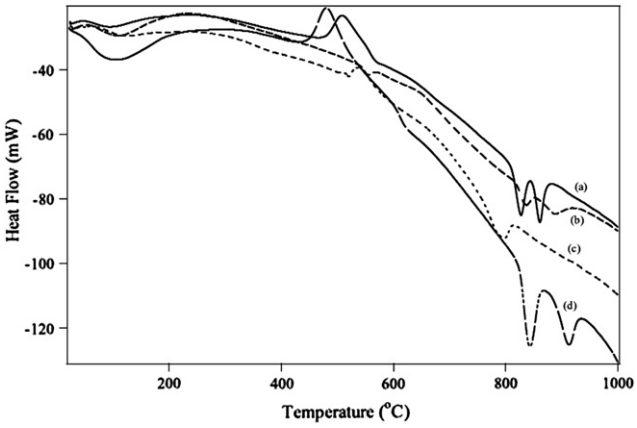

Fig. 5 – The DSC profiles of: (a) AMO (b) $CuMnO_{x-10}$ (c) $CuMnO_{x-15}$, and (d) $CuMnO_{x-5}$ samples.

Fig. 6 shows representative TPD profiles of the AMO sample during heating in a flow of He from room temperature to 1000 °C. These TPD profiles suggest that the TGA weight loss between 25 and 250 °C can be attributed to the loss of physically adsorbed water from the surface of the materials. The weight loss between 250 and 500 °C is primarily due to desorption of CO_2 (presumably from decomposition of carbonaceous species) from these materials. The weight loss between 500 and 1000 °C can be ascribed to evolution of oxygen and more CO_2 from the samples.

3.1.3. *Textural properties*

Representative N_2 adsorption/desorption isotherms of materials synthesized via the redox method are shown in Fig. 7. All the samples exhibited type IV isotherms (IUPAC classification) with distinct hysteresis loops at high relative pressures (>0.45) revealing the mesoporous nature of these materials. The BET surface areas, average pore size, and total pores volumes of prepared materials are shown in Table 1. The synthesized materials had comparable and remarkably high (>268 m^2/g) surface areas. The BJH average pore diameters of these materials ranged from 4.1 to 6.4 nm confirming their

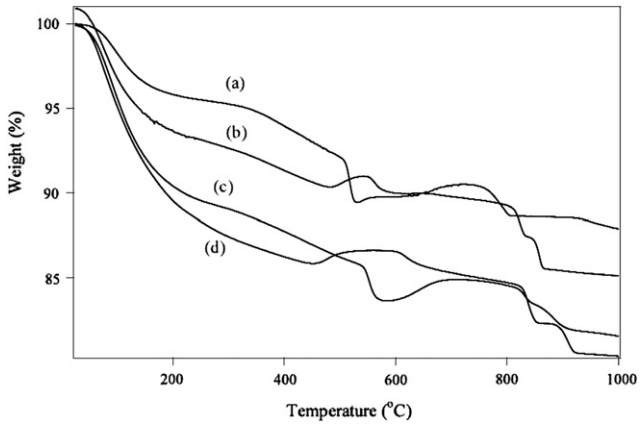

Fig. 4 – The TGA profiles of: (a) $CuMnO_{x-15}$ (b) AMO (c) $CuMnO_{x-10}$, and (d) $CuMnO_{x-5}$ samples.

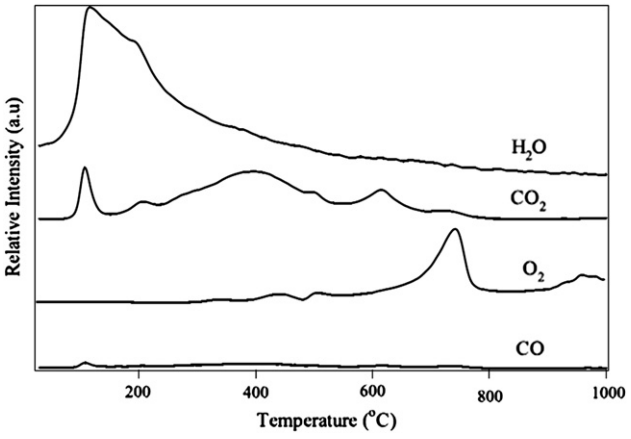

Fig. 6 – The TPD profiles of AMO sample heated in a stream of UHP helium.

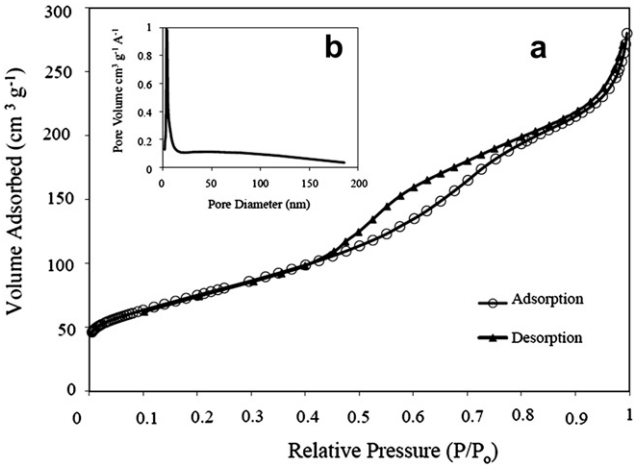

Fig. 7 – (a) N_2 adsorption/desorption isotherms and (b) Barrett–Joyner–Halenda (BJH) desorption pore size distribution plot of the $CuMnO_{x-10}$ sample.

mesoporous nature. The $CuMnO_{x-10}$ catalyst had pores with the largest diameter (6.4 nm) and the highest pore volume (0.45 cm^3/g). These mesopores might play a role in the catalytic activity of the prepared materials.

3.1.4. *Composition of the catalysts*

The molar concentrations (Table 2) of metallic elements as determined by the FAAS method indicate that manganese is the primary constituent of the synthesized materials. The concentration of copper in the catalysts is slightly higher than the nominal values because the preparation method uses an excess amount of copper [44]. The [Cu]/[Mn] ratio in $CuMnO_{x-5}$, $CuMnO_{x-10}$, and $CuMnO_{x-15}$ was 0.06, 0.13, and 0.21, respectively.

3.1.5. *Temperature programmed desorption/reduction (TPD/R)*

The TPD analysis was performed to investigate the adsorption–desorption behavior of the synthesized materials. The CO-TPD profiles are shown in Fig. 8. All samples exhibited broad CO_2 ($m/z = 44$) desorption peaks centered at about 120, 410, 510, and 650 °C. Desorption of CO_2 in the absence of oxygen in the feed stream indicates that the lattice oxygen is involved in CO oxidation. AMO and $CuMnO_{x-10}$ had a relatively small CO_2 desorption peak at 510 °C compared to $CuMnO_{x-5}$ and $CuMnO_{x-15}$ samples. Significant amounts of lattice oxygen are removed and used for CO oxidation even at near ambient temperatures, which might in part account for the high catalytic activity of these materials.

Table 1 – Textural properties of prepared materials.

Samples	BET surface area (m^2/g)	Pore diameter (nm)	Pore volume (cm^3/g)[a]
AMO	275	4.2	0.31
$CuMnO_{x-5}$	268	4.1	0.29
$CuMnO_{x-10}$	271	6.4	0.45
$CuMnO_{x-15}$	270	4.4	0.32

a BJH desorption cumulative pore volume.

Table 2 – Concentration of metallic elements in prepared materials (determined by the FAAS method).

Sample	Concentration (molar %)			[Cu]/[Mn] ratio
	Mn	Cu	K	
AMO	87.8	0	12.2	0
$CuMnO_{x-5}$	82.0	5.3	12.7	0.06
$CuMnO_{x-10}$	83.7	10.5	5.8	0.13
$CuMnO_{x-15}$	78.3	16.2	5.5	0.21

Fig. 9 shows the H_2-TPD profiles of AMO and the $CuMnO_{x-10}$ sample. Desorption of water ($m/z = 18$) reveals the involvement of lattice oxygen in H_2 oxidation. AMO and $CuMnO_{x-10}$ exhibited a broad desorption peak centered at about 300 and 320 °C, respectively. Desorption of water was not observed at temperatures below 100 °C but only became pronounced at temperatures higher than 200 °C.

The combined CO- and H_2-TPD profiles of AMO and the $CuMnO_{x-10}$ sample are shown in Fig. 10. The AMO profiles shows one sharp CO_2 desorption peak at 210 °C, and continuous desorption of water from 210 to 700 °C. On the other hand, the CO_2 profile of $CuMnO_{x-10}$ shows four desorption peaks centered at about 80, 350, 480, and 600 °C. These peaks are shifted to lower temperatures compared to peaks in the CO-TPD profile of $CuMnO_{x-10}$, suggesting that the presence of adsorbed H_2 influences the reaction between CO and lattice oxygen. The H_2O profile shows a broad desorption peak similar to the H_2-TPD peak of the $CuMnO_{x-10}$ sample. The $CuMnO_{x-10}$ profiles reveal that CO_2 desorbed preferentially at temperatures lower than 120 °C. Significant amounts of H_2O desorbed only at temperatures higher than 200 °C.

Fig. 11 shows the CO-TPR profiles of AMO, Hopcalite, and the $CuMnO_{x-10}$ sample. The AMO profile has three reduction peaks centered at ca. 250, 320, and 480 °C. The $CuMnO_{x-10}$ profile also has three reduction peaks centered at ca. 210, 330, and 410 °C. The profile of commercial Hopcalite has three

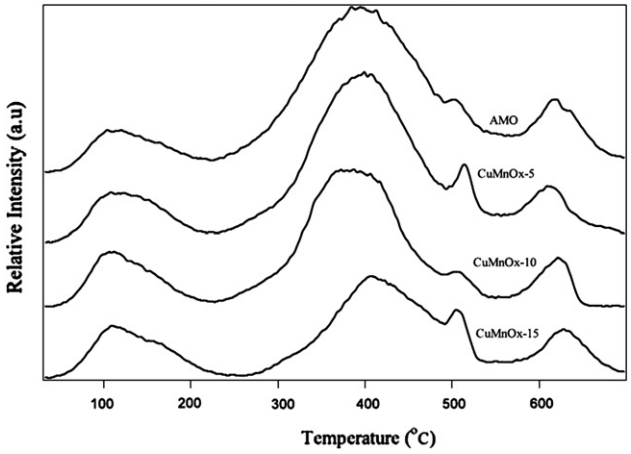

Fig. 8 – The CO_2 ($m/z = 44$) desorption profiles of AMO and copper manganese oxides prepared by the redox method.

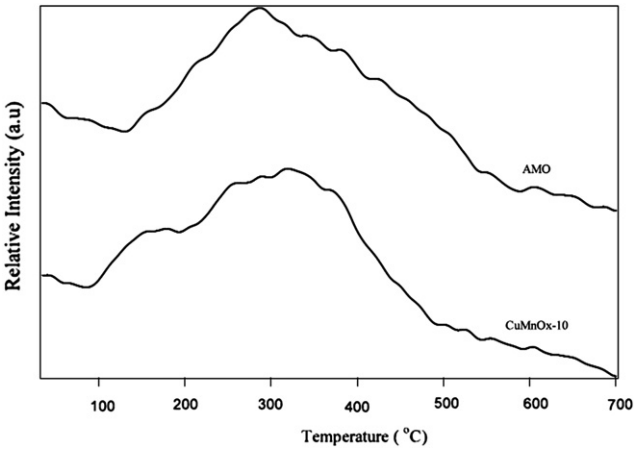

Fig. 9 – H_2-TPD ($m/z = 18$) profiles of AMO and the $CuMnO_{x-10}$ sample.

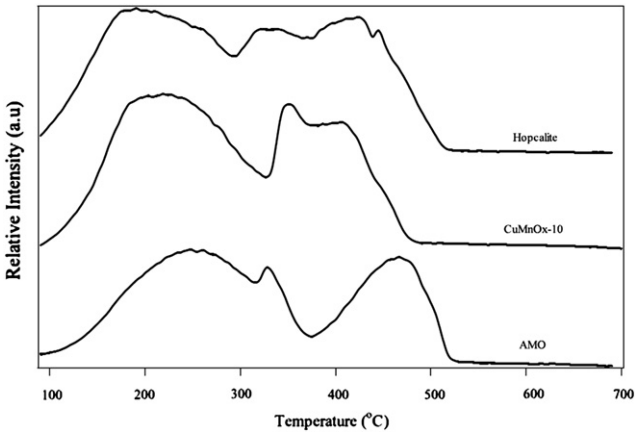

Fig. 11 – The CO-TPR profiles of AMO, $CuMnO_{x-10}$, and hopcalite samples.

reduction peaks centered at ca. 200, 320, and 420 °C. Closer examination of the CO-TPR profiles shows that the first (ca. 250 °C) reduction peak of AMO is shifted to higher temperature relative to the corresponding peaks of $CuMnO_{x-10}$ and commercial Hopcalite. This suggests that the incorporation of copper in the AMO matrix increased the ease of removal of lattice oxygen species from the resultant bimetallic copper manganese oxides. The first $CuMnO_{x-10}$ reduction peak (ca. 210 °C) is significantly larger than corresponding AMO and Hopcalite peaks suggesting a more facile evolution of oxygen species from the $CuMnO_{x-10}$ sample.

3.2. *Catalytic performance*

3.2.1. *Catalytic activity of various catalysts*

The catalytic performance of the synthesized materials in the preferential oxidation of CO is shown in Fig. 12. As shown in Fig. 12(a), AMO exhibited the lowest catalytic activity and was only able to completely oxidize CO at temperatures higher than 125 °C. Incorporating copper improved the catalytic activity of the resultant bimetallic oxides significantly and decreased the temperature for complete CO conversion by 75 °C. $CuMnO_{x-10}$ was the most active catalyst suggesting that the maximum copper loading was about 10% of the total metal content in the samples.

The selectivity to CO oxidation of the synthesized materials at various temperatures is shown in Fig. 12(b). The $CuMnO_{x-10}$ catalyst exhibited the largest (25–75 °C) temperature window for complete and selective oxidation of CO to CO_2. Generally, selectivity decreased with increase of the reaction temperature due to H_2 oxidation. Notably, the oxidation of H_2 only started after the CO in the feed had been completely oxidized. On the basis of its high catalytic activity (100% CO conversion at ambient and subsequent temperatures) and selectivity (100% between 25 and 75 °C) the $CuMnO_{x-10}$ sample was chosen for further rigorous studies.

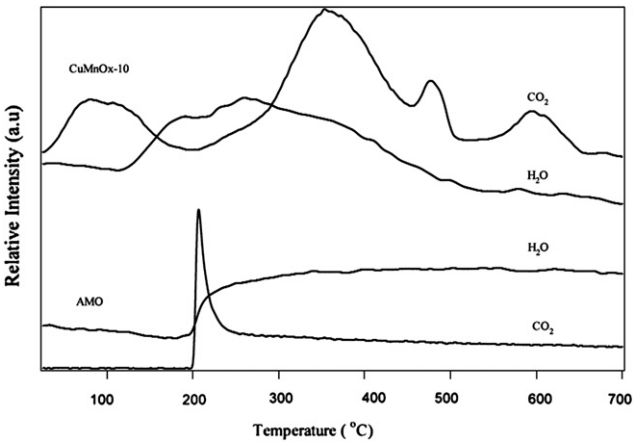

Fig. 10 – The combined CO- and H_2-TPD profiles of AMO and $CuMnO_{x-10}$ samples.

3.2.2. *Effects of H_2, CO_2 and H_2O on catalytic performance*

The catalytic performance of the $CuMnO_{x-10}$ sample under diverse conditions is shown in Fig. 13. As shown in Fig. 13(a), $CuMnO_{x-10}$ catalyst completely oxidized CO in the whole temperature range both with and without H_2 in the feed gas. The presence of 60% H_2 in the feed did not affect CO conversion in the whole temperature range. However, the presence of 25% CO_2 in the feed drastically reduced the conversion of CO at ambient temperature. Moreover, adding ~ ~3% H_2O into the feed containing 25% CO_2 reduces the conversion of CO at low temperatures even further and increases the temperature at which complete conversion occurs by 50 °C.

When the feed gas had no H_2 the only reaction that occurred was CO oxidation in which case the selectivity towards CO oxidation is always 100%. However, with a feed gas containing 60% H_2 the selectivity decreased continuously with temperature starting at 75 °C as shown in Fig. 13(b). This indicates that the rate of H_2 oxidation increased with temperature consuming an increasing portion of oxygen in the feed. The presence of CO_2 and H_2O in the feed did not have any significant effect on selectivity. However, the presence of H_2O in the feed shifted the selectivity curve to higher temperatures due to reduced catalytic activity.

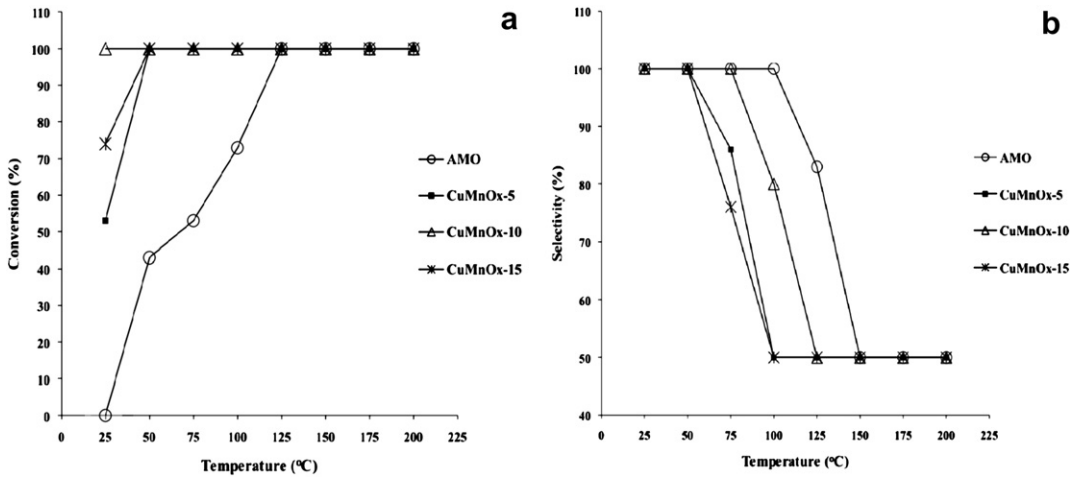

Fig. 12 – Catalytic performance of synthesized materials in preferential oxidation of CO: (a) CO conversion (b) O_2 selectivity to CO oxidation. Space velocity: 35,000 mL h^{-1} g_{cat}^{-1}, feed gas: 1% CO, 1% O_2, 60% H_2 in N_2.

3.2.3. *Effect of CO concentration*

The effects of CO concentration on the catalytic performance of $CuMnO_{x-10}$ sample are presented in Fig. 14. There was no substantial difference in catalytic activity when the concentration of CO in the feed gas was 0.5 and 1% as shown in Fig. 14(a). However, CO conversion decreased significantly at low temperatures (<100 °C) when the concentration of CO in the feed was 2%. As shown in Fig. 14(b) when the feed gas contained stoichiometric amounts of O_2 and CO the selectivity was 100% in the whole temperature range (25–200 °C). However, selectivity decreased considerably at high temperatures (>75 °C) with a feed gas containing excess oxygen suggesting the presence of CO in the feed had an inhibitory effect on H_2 oxidation. Consequently, the oxidation of H_2 only started when CO in the feed gas had been completely oxidized. All the excess O_2 in the feeds was used to oxidize H_2 starting at 125 °C and subsequent higher temperatures.

3.2.4. *Effect of O_2 concentration*

Fig. 15 shows the effects of O_2 concentration on the catalytic performance of the $CuMnO_{x-10}$ sample. As shown in Fig. 15(a) CO conversion was significantly higher (100%) at low temperatures (50–125 °C) with excess O_2 in the feed gas. The CO conversion was considerably lower (<100%) at low temperatures (50–125 °C) with stoichiometric O_2 in the feed gas. The selectivity was 100% over the entire temperature range (Fig. 15(b)) with stoichiometric amount of O_2 in the feed demonstrating that CO was preferentially oxidized even at high temperatures. The selectivity dropped significantly at temperatures higher than 75 °C when the feed had excess amount of oxygen due to H_2 oxidation. However, no H_2 oxidation was observed as long as CO was present in the feed.

3.2.5. *Effect of space velocity*

Fig. 16 shows catalytic performance of the $CuMnO_{x-10}$ sample at different space velocities. As shown in Fig. 16(a) CO conversion decreased with increasing space velocity at low temperatures (<100 °C). Complete conversion could be obtained only at temperatures 100 °C and above at the space velocity of 70 000 mL h^{-1} g_{cat}^{-1}. The space velocity did not have any significant effect on selectivity as shown in Fig. 16(b). The decrease in catalytic activity at the space velocity of

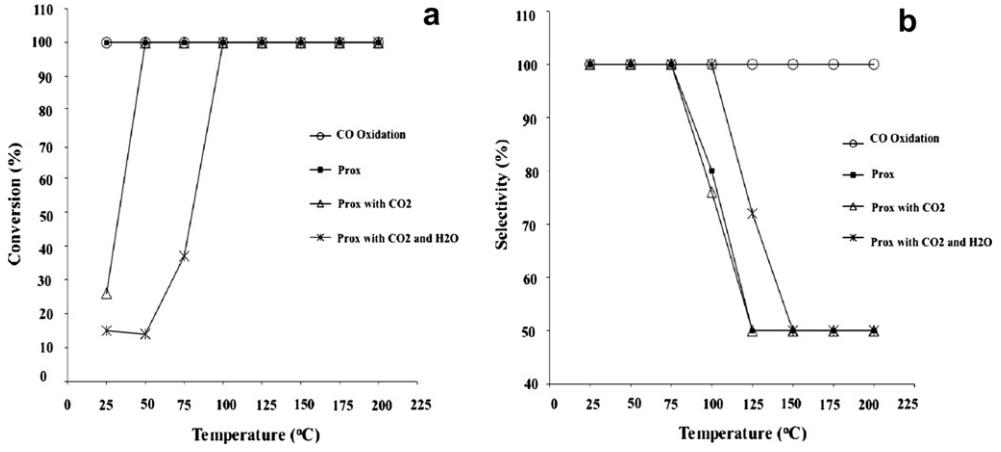

Fig. 13 – Catalytic performance of the $CuMnO_{x-10}$ sample under various conditions: (a) CO conversion (b) selectivity. Space velocity: 35,000 mL h^{-1} g_{cat}^{-1}, feed gas: CO oxidation (1% CO + 1% O_2 in N_2), Prox (1% CO + 1% O_2 + 60% H_2 in N_2).

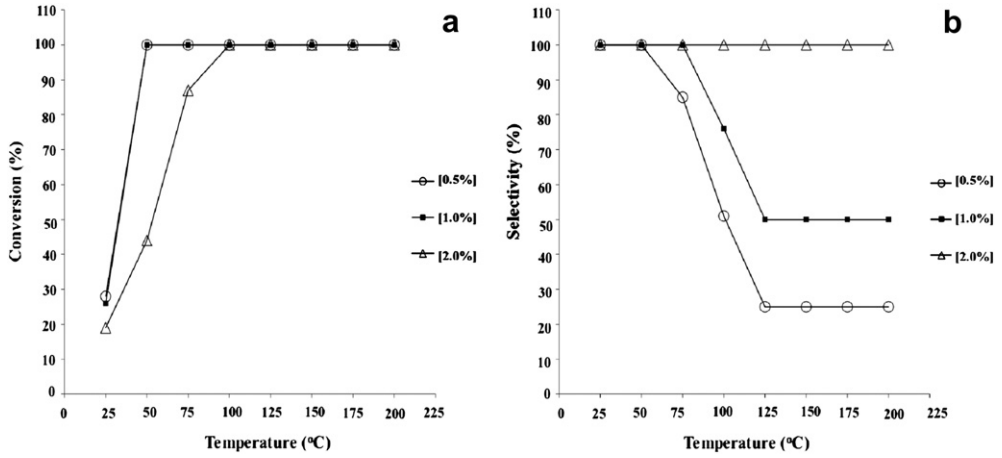

Fig. 14 – Effects of CO concentration on catalytic performance of the $CuMnO_{x-10}$ sample: (a) CO conversion (b) selectivity. Space velocity: 35,000 mL h^{-1} g_{cat}^{-1}, feed gas: CO (shown), 1% O_2, 25% CO_2, 60% H_2 in N_2.

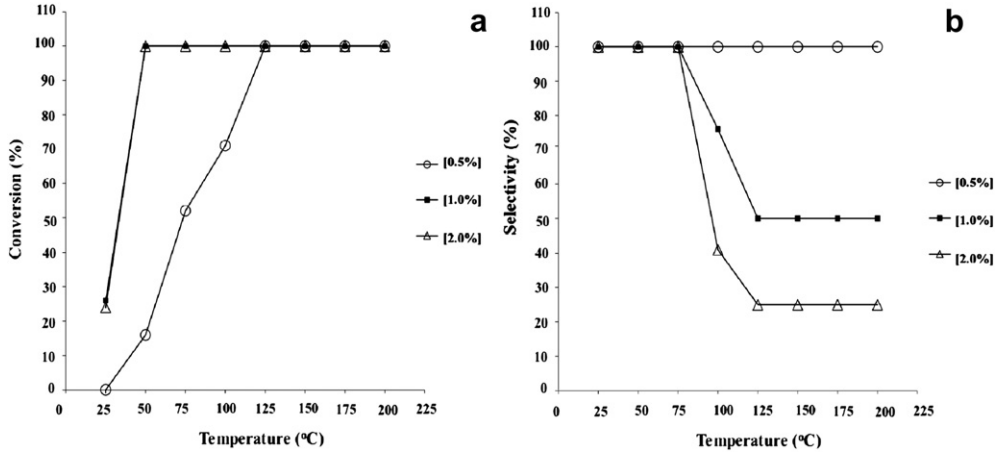

Fig. 15 – Effects of O_2 concentration on the catalytic performance of $CuMnO_{x-10}$ sample: (a) CO conversion (b) selectivity. Space velocity: 35,000 mL h^{-1} g_{cat}^{-1}, feed gas: 1% CO, O_2 (shown), 25% CO_2, 60% H_2 in N_2.

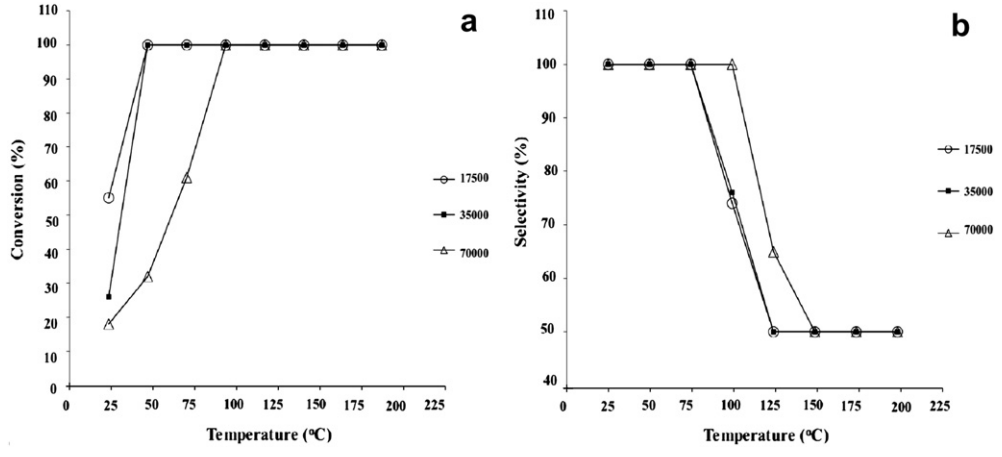

Fig. 16 – Effects of space velocity on catalytic performance of $CuMnO_{x-10}$ sample: (a) CO conversion (b) selectivity. Feed gas: 1% CO, 1% O_2, 25% CO_2, 60% H_2 in N_2.

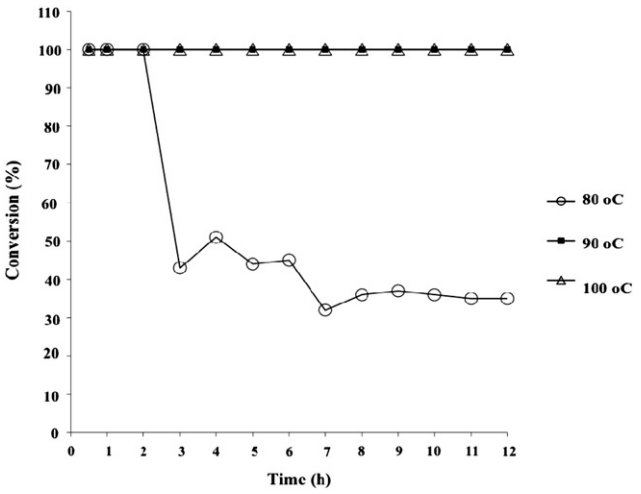

Fig. 17 – Effects of reaction time on the catalytic performance of $CuMnO_{x-10}$ sample at different temperatures. Space velocity: 35,000 mL h^{-1} g_{cat}^{-1}, feed gas: 1% CO, 1% O_2, 3% H_2O, 25% CO_2, 60% H_2 in N_2.

70 000 mL h^{-1} g_{cat}^{-1} shifted the selectivity curve to higher temperatures by about 25 °C.

3.2.6. *Stability studies*

Stability studies were performed using a feed gas containing both CO_2 and H_2O in order to investigate the performance of copper manganese oxide catalysts under realistic fuel cell conditions. Fig. 17 shows the catalytic performance with time on-stream for the $CuMnO_{x-10}$ sample. No catalytic decay was observed after 12 h on-stream when reactions were performed at 90 and 100 °C. CO conversion decreased drastically after a few hours time on-stream when the reaction was performed at 80 °C presumably due to water poisoning, since CO_2 had no observable effect on catalytic performance at 80 °C (see Fig. 13).

4. Discussion

The catalytic performance of binary copper manganese oxides is influenced by a combination of factors including the preparation method, surface area, crystallinity, and copper loading. Copper manganese oxides with high surface areas and low crystallinity have been found to be highly active for CO oxidation [40,46,47].

Several factors are responsible for the high catalytic activity of materials synthesized using the redox method. The FE-SEM and TEM analyses reveal the presence of aggregates of microparticles made of packed fibrous nanoscale particles. This type of morphology can lead to the presence of a large number of adsorption sites in the synthesized materials. The BET analysis shows that the synthesized materials are porous and have very high surface areas (>268 m^2/g), which leads to high sorption capacity and the presence of a large number of active sites. Structural defects resulting from the poor crystallinity of these materials as revealed by the SAED analysis can lead to the presence of oxygen vacancies, which can provide adsorbing centers for oxygen, enhancing the oxidative activity of these materials. The CO-TPD results reveal that CO oxidation started at near ambient temperatures with substantial CO oxidation occurring below 100 °C. This indicates the lattice oxygen is readily available for CO oxidation. In addition, the activation energy for CO oxidation on the surface of materials prepared by the redox method is low, which also accounts for their high intrinsic catalytic activity.

The CO-TPR results show the presence of three reduction peaks in the materials. The first reduction peak for AMO is centered at a higher temperature (ca. 250 °C) relative to those of $CuMnO_{x-10}$ and Hopcalite. This suggests that copper has a promotional effect on manganese reduction. The shifting of the reduction temperature to lower temperature (ca. 210 °C) on incorporation of copper indicates increased ease of removal of lattice oxygen species.

The catalytic activity of AMO was significantly less than that of copper manganese oxides suggesting that the incorporation of copper into the AMO framework enhanced the catalytic activity of the resultant bimetallic oxides. Previous studies [41,43,44] indicate that the incorporation of copper enhances the catalytic performance by increasing the mobility and ease of release of lattice oxygen. The optimum copper loading in samples prepared using the redox method was about 10% of the total metal content in the samples. Other studies [40,46,48,49] have observed activity maxima at copper loadings of 10, 20, and 50%.

The compositional homogeneity of binary copper manganese oxides is a critical determinant of their catalytic activity. Recently, Tang et al. [50] prepared copper manganese oxide catalysts using the supercritical antisolvent precipitation method and found them to have a significantly higher catalytic activity for CO oxidation than conventionally prepared Hopcalite. They attributed the high intrinsic catalytic activity (more than twice as active per unit surface area as the conventionally prepared hopcalite catalysts) to the nanocrystalline homogeneous nature of the synthesized catalysts, which brought the active components together in the same phase.

Morphological analysis of copper manganese oxides synthesized using the redox method suggests they are compositionally homogeneous. The morphological uniformity (examined by FE-SEM and TEM) and the largely homogeneous elemental distribution (examined by STEM) indicate there was intimate intermixing of Mn, Cu, and O leading to compositionally homogeneous nanoscale materials. This was presumably due to the dropwise addition of a solution containing a mixture of Mn^{2+} and Cu^{2+} ions to a solution of $KMnO_4$ and the subsequent aging for 24 h with continuous stirring leading to a uniform incorporation of Cu^{2+} ions in the resultant amorphous manganese oxide framework. Subsequent calcination of the copper manganese oxide precursors in air at 300 °C converted the Cu^{2+} ions into CuO to form compositionally homogeneous binary copper manganese oxides with high intrinsic catalytic activity.

Samples prepared using the redox method were amorphous and highly selective for CO oxidation. The CO-TPD analysis reveals that CO oxidation started from ambient temperature with significant CO oxidation occurring at about 110 °C. On the other hand, H_2-TPD results show that no H_2

oxidation occurred at temperatures below 100 °C. H_2 oxidation became pronounced only at temperatures higher than 200 °C. Results of TPD studies using a mixture of CO and H_2 reveals that CO oxidation occurred preferentially at temperatures below 110 °C. These TPD results indicate that the activation energy of H_2 oxidation is higher than that of CO oxidation, which is the major reason for the high selectivity of these catalysts.

The TPD results show that both CO and H_2 oxidation occurred in the absence of oxygen in the gas feed, indicating that lattice oxygen is involved in the oxidation process. The involvement of lattice oxygen in the oxidation process suggests that the oxidation proceeds via the Mars van Krevelen mechanism. CO adsorbs on the catalyst surface and reacts with lattice oxygen to form CO_2 that desorbs. The resulting oxygen vacancies are subsequently refilled by oxygen from the feed gas. An analogous mechanism can also be used to describe H_2 oxidation.

The presence of CO_2 and H_2O in the feed gas significantly decreased the catalytic performance of copper manganese oxides at lower (<50 °C) temperatures. Carbon dioxide and water inhibit catalytic activity by adsorbing on the active sites [44,51]. The inhibitory effect becomes less pronounced at temperatures higher than 75 °C because the rate of CO_2 and H_2O desorption increases.

The catalytic activity of $CuMnO_{x-10}$ sample decreased significantly at temperatures lower than 100 °C at higher space velocity (70 000 mL h^{-1} g_{cat}^{-1}). However, even at this very high space velocity, complete conversion of CO was observed at the temperature (100 °C) of PEM fuel cells suggesting copper manganese oxide catalysts are promising for PEM fuel cells applications.

5. Conclusions

Mesoporous copper manganese oxide catalysts were synthesized at room temperature using a simple redox method. These bimetallic oxides showed remarkable catalytic activity (100% at $\geq$ 50 °C) and high selectivity (100% with stoichiometric reactants) for CO oxidation in H_2-rich feed streams. The high catalytic activity was attributed to a combination of factors including high surface areas (>268 m^2/g), low crystallinity, compositional homogeneity, low activation energy, and the presence of readily available lattice oxygen for CO oxidation. The high selectivity was attributed to the significantly lower activation energy for CO oxidation compared to the activation energy for H_2 oxidation. These materials are CO_2 and H_2O tolerant when reaction temperatures are higher than 90 °C making them potentially useful in the removal of CO in low and medium temperature PEM fuel cells.

Acknowledgements

The authors thank Dr. Roger Ristau and Dr. Lichun Zhang for assisting with microscopy experiments. We would also like to thank Laura Pinnati for help with TGA/DSC analysis.

We gratefully acknowledge financial support from the US Department of Energy, Office of Basic Energy Sciences, Division of Chemical Sciences, Geosciences, and Biological Sciences.

REFERENCES

[1] Gottesfeld S, Pafford J. A new approach to the problem of carbon monoxide poisoning in fuel cells operating at low temperatures. J Electrochem Soc 1988;135:2651–2.
[2] Ahluwalia RK, Zhang Q, Chmielewski DJ, Lauzze KC, Inbody MA. Performance of CO preferential oxidation reactor with noble-metal catalyst coated on ceramic monolith for on-board fuel processing applications. Catal Today 2005;99:271–83.
[3] Gu C, Lu S, Miao J, Liu Y, Wang Y. Meso-macroporous monolithic CuO–CeO_2/γ/α–Al_2O_3 catalysts for CO preferential oxidation in hydrogen-rich gas: effect of loading methods. Int J Hydrogen Energy 2010;35:6113–22.
[4] Martínez-Arias A, Hungría AB, Munuera G, Gamarra D. Preferential oxidation of CO in rich H_2 over CuO/CeO_2: details of selectivity and deactivation under the reactant stream. Appl Catal B 2006;65:207–16.
[5] Springer TE, Rockward T, Zawodzinski TA, Gottesfeld S. Model for polymer electrolyte fuel cell operation on reformate feed: effects of CO, H_2 dilution, and high fuel utilization. J Electrochem Soc 2001;148:A11–23.
[6] Zamel N, Li X. Transient analysis of carbon monoxide poisoning and oxygen bleeding in a PEM fuel cell anode catalyst layer. Int J Hydrogen Energy 2008;33:1335–44.
[7] Chen YZ, Liaw BJ, Chang WC, Huang CT. Selective oxidation of CO in excess hydrogen over CuO/$Ce_xZr_{1-x}O_2$–Al_2O_3 catalysts. Int J Hydrogen Energy 2007;32:4550–8.
[8] Kahlich MJ, Gasteiger HA, Behm RJ. Kinetics of the selective low-temperature oxidation of CO in H_2-rich gas over Au/α–Fe_2O_3. J Catal 1999;182:430–40.
[9] Brett DJL, Aguiar P, Brandon NP, Kucernak AR. Measurement and modelling of carbon monoxide poisoning distribution within a polymer electrolyte fuel cell. Int J Hydrogen Energy 2007;32:863–71.
[10] Lu S, Zhang C, Liu Y. Carbon nanotube supported Pt–Ni catalysts for preferential oxidation of CO in hydrogen-rich gases. Int J Hydrogen Energy 2011;36:1939–48.
[11] Luengnaruemitchai A, Nimsuk M, Naknam P, Wongkasemjit S, Osuwan S. A comparative study of synthesized and commercial A-type zeolite-supported Pt catalysts for selective CO oxidation in H_2-rich stream. Int J Hydrogen Energy 2008;33:206–13.
[12] Souza MMVM, Ribeiro NFP, Schmal M. Influence of the support in selective CO oxidation on Pt catalysts for fuel cell applications. Int J Hydrogen Energy 2007;32:425–9.
[13] Oh SH, Sinkevitch RM. Carbon monoxide removal from hydrogen-rich fuel cell feedstreams by selective catalytic oxidation. J Catal 1993;142:254–62.
[14] Kahlich MJ, Gasteiger HA, Behm RJ. Kinetics of the selective CO oxidation in H_2-rich gas on Pt/Al_2O_3. J Catal 1997;171:93–105.
[15] Manasilp A, Gulari E. Selective CO oxidation over Pt/alumina catalysts for fuel cell applications. Appl Catal B 2002;37:17–25.
[16] Han YF, Kahlich MJ, Kinne M, Behm RJ. Kinetic study of selective CO oxidation in H_2-rich gas on a Ru/γ–Al_2O_3 catalyst. Phys Chem Chem Phys 2002;4:389–97.
[17] Echigo M, Tabata T. A study of CO removal on an activated Ru catalyst for polymer electrolyte fuel cell applications. Appl Catal A Gen 2003;251:157–66.

[18] Echigo M, Tabata T. Development of novel Ru catalyst of preferential CO oxidation for residential polymer electrolyte fuel cell systems. Catal Today 2004;90:269–75.
[19] Han YF, Kahlich MJ, Kinne M, Behm RJ. CO removal from realistic methanol reformate via preferential oxidation-performance of a Rh/MgO catalyst and comparison to Ru/γ–Al_2O_3, and Pt/γ–Al_2O_3. Appl Catal B 2004;50:209–18.
[20] Galletti C, Specchia S, Saracco G, Specchia V. CO preferential oxidation in H_2-rich gas for fuel cell applications: microchannel reactor performance with Rh-based catalyst. Int J Hydrogen Energy 2008;33:3045–8.
[21] Galletti C, Specchia S, Saracco G, Specchia V. Catalytic performance of rhodium-based catalysts for CO preferential oxidation in H_2-rich gases. Ind Eng Chem Res 2008;47: 5304–12.
[22] Sanchez RMT, Ueda A, Tanaka K, Haruta M. Selective oxidation of CO in hydrogen over gold supported on manganese oxides. J Catal 1997;168:125–7.
[23] Grisel RJH, Nieuwenhuys BE. Selective oxidation of CO, over supported Au catalysts. J Catal 2001;199:48–59.
[24] Luengnaruemitchai A, Osuwan S, Gulari E. Selective catalytic oxidation of CO in the presence of H_2 over gold catalyst. Int J Hydrogen Energy 2004;29:429–35.
[25] Chang L, Yeh Y, Chen Y. Preferential oxidation of CO in hydrogen stream over nano-gold catalysts prepared by photodeposition method. Int J Hydrogen Energy 2008;33: 1965–74.
[26] Tu Y, Luo J, Meng M, Wang G, He J. Ultrasonic-assisted synthesis of highly active catalyst Au/MnO_x–CeO_2 used for the preferential oxidation of CO in H_2-rich stream. Int J Hydrogen Energy 2009;34:3743–54.
[27] Yang Y, Sangeetha P, Chen Y. Au/TiO_2 catalysts prepared by photo-deposition method for selective CO oxidation in H_2 stream. Int J Hydrogen Energy 2009;34:8912–20.
[28] Ng JWD, Zhong Z, Luo J, Borgna A. Enhancing preferential oxidation of CO in H_2 on Au/α–Fe_2O_3 catalyst via combination with APTES/SBA-15 CO_2-sorbent. Int J Hydrogen Energy 2010;35:12724–32.
[29] Avgouropoulos G, Ioannides T. Selective CO oxidation over CuO–CeO_2 catalysts prepared via the urea-nitrate combustion method. Appl Catal A Gen 2003;244:155–67.
[30] Liu Y, Fu Q, Stephanopoulos MF. Preferential oxidation of CO in H_2 over CuO–CeO_2 catalysts. Catal Today 2004;93-95: 241–6.
[31] Bae CM, Ko JB, Kim DH. Selective catalytic oxidation of carbon monoxide with carbon dioxide, water vapor and excess hydrogen on CuO–CeO_2 mixed oxide catalysts. Catal Commun 2005;6:507–11.
[32] Mariño F, Baronetti G, Laborde M, Bion N, Valant AL, Epron F, et al. Optimized CuO–CeO_2 catalysts for COPROX reaction. Int J Hydrogen Energy 2008;33:1345–53.
[33] Liu Z, Zhou R, Zheng X. Influence of residual K^+ on the catalytic performance of CuO–CeO_2 catalysts in preferential oxidation of CO in excess hydrogen. Int J Hydrogen Energy 2008;33:791–6.
[34] Lee HC, Kim DH. Kinetics of CO and H_2 oxidation over CuO–CeO_2 catalyst in H_2 mixtures with CO_2 and H_2O. Catal Today 2008;132:109–16.
[35] Moreno M, Baronetti GT, Laborde MA, Mariño FJ. Kinetics of preferential CO oxidation in H_2 excess (COPROX) over CuO/CeO_2 catalysts. Int J Hydrogen Energy 2008;33:3538–42.
[36] Teng Y, Sakurai H, Ueda A, Kobayashi T. Oxidative removal of CO contained in hydrogen by using metal oxide catalysts. Int J Hydrogen Energy 1999;24:355–8.
[37] Merrill DR, Scalione CC. The catalytic oxidation of carbon monoxide at ambient temperature. J Am Chem Soc 1921;43: 1982–2002.
[38] Brittan MA, Bliss H, Walker CA. Kinetics of hopcalite-catalyzed oxidation of carbon monoxide. AlChE J 1970;16: 305–14.
[39] Yoon C, Cocke DL. The design and preparation of planar models of oxidation catalysts: I. Hopcalite. J Catal 1988;113: 267–80.
[40] Krämer M, Schmidt T, Stöwe K, Maier WF. Structural and catalytic aspects of sol–gel derived copper manganese oxides as low-temperature CO oxidation catalyst. Appl Catal A Gen 2006;302:257–63.
[41] Hasegawa YI, Maki RU, Sano M, Miyake T. Preferential oxidation of CO on copper-containing manganese oxides. Appl Catal A Gen 2009;371:67–72.
[42] Valdés-Solís T, López I, Marbán G. Copper manganite as a catalyst for the PROX reaction. Deactivation studies. Int J Hydrogen Energy 2010;35:1879–87.
[43] Hernández WY, Centeno MA, Romero-Sarria F, Ivanova S, Montes M, Odriozola JA. Modified cryptomelane-type manganese dioxide nanomaterials for preferential oxidation of CO in the presence of hydrogen. Catal Today 2010;157:160–5.
[44] Njagi EC, Chen CH, Genuino H, Galindo H, Huang H, Suib SL. Total oxidation of CO at ambient temperature using copper manganese oxide catalysts prepared by a redox method. Appl Catal B 2010;99:103–10.
[45] Avgouropoulos G, Ioannides T. Effect of synthesis parameters on catalytic properties of CuO–CeO_2. Appl Catal B 2006;67:1–11.
[46] Kanungo SB. Physicochemical properties of MnO_2 and MnO_2–CuO and their relationship with the catalytic activity for H_2O_2 decomposition and CO oxidation. J Catal 1979;58: 419–35.
[47] Hutchings GJ, Mirzaei AA, Joyner RW, Siddiqui MRH, Taylor SH. Effect of preparation conditions on the catalytic performance of copper manganese oxide catalysts for CO oxidation. Appl Catal A Gen 1998;166:143–52.
[48] Dollimore D, Tonge KH. The constitution and oxidizing properties of materials in the copper(II) oxide-manganese(III) oxide system. J Chem Soc A; 1970:1728–31.
[49] Hasegawa Y, Fukumoto K, Ishima T, Yamamoto H, Sano M, Miyake T. Preparation of copper-containing mesoporous manganese oxides and their catalytic performance for CO oxidation. Appl Catal B 2009;89:420–4.
[50] Tang ZR, Jones CD, Aldridge JKW, Davies TE, Bartley JK, Carley AF, et al. New nanocrystalline Cu/MnO_x catalysts prepared from supercritical antisolvent precipitation. Chem Cat Chem 2009;1:247–51.
[51] Veprek S, Cocke DL, Kehl S, Oswald HR. Mechanism of the deactivation of Hopcalite catalysts studied by XPS, ISS, and other techniques. J Catal 1986;100:250–63.